

# Performance and Design Scaling of Magnetoshells for Outer Planet Drag-Modulated Plasma Aerocapture

Charles L. Kelly and Justin M. Little  
University of Washington SPACE Lab  
Seattle, WA 98105  
clk1391@uw.edu

**Abstract**—The application of drag-modulated plasma aerocapture (DMPA) to outer planet orbiter missions is analyzed in terms of performance results and spacecraft design scaling. The magnetoshell, a magnetized plasma used in place of an aeroshell, generates drag by ionizing, capturing, and magnetically deflecting the atmospheric flow. The plasma is sustained by in-situ gas and kinetic energy at velocities above a certain threshold, which is in excess of 15 km/s for hydrogen flow. The magnetoshell drag is shown to scale with magnetic field strength, enabling continuous modulation of the ballistic coefficient via control of the electrical current to the magnet. A design framework for generating preliminary DMPA mission architectures is presented and a sample design is compared to an existing Neptune orbiter concept that uses an ADEPT drag skirt. Compared to ADEPT, the DMPA architecture is shown to deliver 70% higher orbiter mass and experience 30% lower stagnation heating. It achieves a ballistic coefficient of  $\beta = 4 \text{ kg/m}^2$  with a ballistic coefficient ratio of  $\beta_{\max}/\beta_{\min} = 67$ , both results indicating a high degree of control authority via the continuous drag modulation scheme. Recommendations for using the design framework to optimize arbitrary DMPA architectures are discussed as well as additional considerations for the technological feasibility of a given magnetoshell design.

The ultimate drag modulation scheme is one that can achieve continuous control over a large range of ballistic coefficient values. Modern aeroshell devices have no reliable mechanism for implementing this type of control. An alternative technology, the magnetoshell, proposes to use a magnetized plasma in place of a physical surface that generates drag by ionizing, capturing, and deflecting atmospheric gas [5]. The interaction is seeded by injecting a small amount of plasma from aboard the spacecraft into the magnetic field. The magnetic field determines the strength of the interaction and therefore the drag force. Controlling the magnetic field strength is a matter of adjusting the current applied to an electromagnet, so the drag force can be modulated continuously without moving parts. Aeroshells generate drag with deployable physical elements (such as [6], [7], [8]) that must stow within the launch vehicle payload fairing. In contrast, although the magnet itself must fit the same constraint, the magnetoshell's effective drag surface is made up of plasma which can extend tens of meters beyond this size. This means magnetoshells can mitigate pressure and heat loads to the spacecraft by enabling trajectories higher in the atmosphere. The magnetoshell plasma is sustained by the trapping of in-situ atmospheric gas and kinetic energy, offering better performance at higher velocity. Thus, they are particularly suited for fast-transfer entries and/or outer planet aerocapture.

## TABLE OF CONTENTS

1. INTRODUCTION .....	1
2. PERFORMANCE MODELING AND SCALING .....	2
3. MISSION DESIGN CONSIDERATIONS .....	4
4. CONCLUSION .....	8
ACKNOWLEDGMENTS .....	9
REFERENCES .....	9
BIOGRAPHY .....	10

## 1. INTRODUCTION

Aerocapture is an orbit insertion maneuver that uses drag of a planetary atmosphere on a spacecraft to slow it from a hyperbolic trajectory to a closed elliptic orbit. Because the spacecraft decelerates without the use of propulsion, this maneuver is proposed to offer significant advantages in delivered payload size, mass savings, and cost reduction [1]. However, risks including atmosphere knowledge uncertainty, entry trajectory inaccuracy, and extreme heat loads have prevented engineers from attempting it in any mission. One mitigation strategy is the use of drag modulation, whereby the ballistic coefficient of the entry vehicle is modified inside the atmosphere to target a final orbit more accurately. Simulations have shown that schemes involving staged jettisoning of aeroshell devices (such as [2], [3]) result in greater final orbit accuracy, with the benefit increasing the more one can control the ballistic coefficient [4].

Despite the promises of Drag-Modulated Plasma Aerocapture (DMPA), its practical use in missions is relatively uncharacterized because of the complexity of modeling and experimentally validating magnetoshell performance. Hancock et al. [9] conducted a systems analysis of DMPA for human-class Mars missions, but this was based on a phenomenological model of magnetoshell drag [10] that treated the plasma as a solid body. Since then, detailed analytical modeling has revealed many physical effects unique to magnetoshells. For instance, the plasma is not a discrete flow impediment but rather interacts with the atmosphere in a diffuse manner [11]. Discontinuous, orders-of-magnitude performance gains have also been observed to occur at critical flow velocity thresholds [12], [13]. This modeling indicates that DMPA offers the greatest advantage for gas and ice giant missions [14] where the extreme entry velocities ( $\sim 20$ – $60 \text{ km/s}$ ) are likely to rule out modern aeroshells and TPS [15]. Furthermore, while continuously-variable drag modulation is theoretically shown to outperform staged jettison schemes [4], there has been no trajectory analysis of DMPA that incorporates these physics in a control law to determine its ability to accurately reach target orbits.

This paper examines the implications of the latest physical modeling on the design of such outer planet DMPA missions. We first review the results of modeling pertaining to magnetoshell performance in a hydrogen environment relevant to ice and gas giant atmospheres. We then present a general framework of magnetoshell systems design that informs the basic elements of a DMPA mission concept. The goal of this

paper is to provide tools to the mission design community that enable consideration of DMPA architectures without the need for an independent plasma physics model or expertise. To this end, we have published a [downloadable dataset](#) of performance modeling results that can be used for design scaling and implementation of continuously-variable drag modulation in trajectory simulation codes.

## 2. PERFORMANCE MODELING AND SCALING

Physics and performance have been characterized previously using an analytical model of the global interaction between the magnetosheath and a hypersonic flow. Here, we briefly recap some key results of modeling (presented comprehensively in [12] and [13]) before discussing performance derived for a hydrogen environment.

### 2.1 Analytical Plasma Model

The analytical model represents the magnetosheath as a plasma confined by a dipole magnetic field produced by a loop of current representing the magnet coil. The plasma is encountered by a rarefied, hypersonic gas flow representing the atmosphere during aerocapture in the reference frame of the magnetosheath. A control volume is defined by the boundary inside which any newly generated ions are confined by the magnetic field. In general, this ion-trapping region grows with higher magnetic field strength and magnet size and shrinks with higher flow velocity and particle mass. We develop a system of fluid conservation equations that describes the exchange of particles and energy between the neutral flow, plasma populations, and additional neutral particles within the plasma. The equations are averaged over the control volume to a form easily solvable by a numerical method within a few seconds on a modern PC. The solutions to the equations give the time evolution of plasma and neutral densities ( $n_i$ ,  $n_e$ ,  $n_{2n}$ ) and temperatures ( $T_i$ ,  $T_e$ ,  $T_{2n}$ ) in the control volume, which are manipulated to reveal underlying physics and performance results.

Presently, the analytical model describes alike atomic particle interactions. Therefore, to model DMPA in an ice or gas giant atmosphere, we make a simplifying approximation of an atomic hydrogen flow. A higher complexity model is under development that will take into account the plasma chemistry of molecular H<sub>2</sub> interactions as a more faithful representation of an ice/giant atmosphere. Future work will further advance the complexity to model other atmospheric species and mixtures of interest (e.g. CO<sub>2</sub>, air). We note that the dissociation energy for H<sub>2</sub> (4.5 eV) is much lower than its ionization energy (16 eV). For the purposes of this study we assume the plasma/neutral interaction is dominated by H-H<sup>+</sup> interactions and include a term in the model that represents dissociation as a loss of electron energy. We re-iterate here that forthcoming work will incorporate the molecular plasma chemistry with higher accuracy.

Fig. 1 shows the results of one simulation with freestream particle density  $n_\infty = 10^{18}/\text{m}^3$ , freestream velocity  $u_\infty = 30 \text{ km/s}$ , magnet radius  $r_c = 1 \text{ m}$ , magnetic field strength  $B_0 = 500 \text{ G}$ , and seed plasma injected power  $P_{\text{inj}} = 50 \text{ W}$ . This figure depicts the distributions of magnetosheath plasma density  $n_i$  and stream density  $n_{sn}$  in equilibrium (i.e. the simulation has evolved to steady state). The magnet axis is aligned with the  $(r, z)$  cylindrical coordinate axis, along which the hypersonic stream flows in the  $+z$  direction. The magnetosheath forms as a donut-shaped plasma around the magnet, reflective of the dipole magnetic field topology.  $n_i$

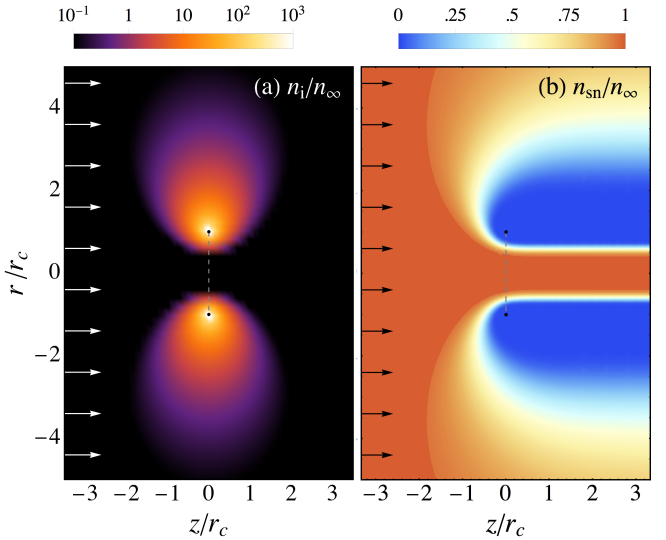


**Figure 1.** The freestream-normalized spatial distributions of (a) plasma density,  $n_i$  and (b) neutral flow density,  $n_{sn}$  demonstrate their coupling. The point at  $(r, z) = (\pm r_c, 0)$  is where the magnet coil intersects the  $r$ - $z$  plane. The fixed conditions are  $n_\infty = 10^{18} \text{ m}^{-3}$ ,  $u_\infty = 30 \text{ km/s}$ ,  $B_0 = 500 \text{ G}$ ,  $r_c = 1 \text{ m}$ , and  $P_{\text{inj}} = 50 \text{ W}$ .

is highest near the magnet and becomes more diffuse radially outward. This results in an interaction with the neutral stream that gradually weakens with  $r$ . The stream density  $n_{sn}$  ranges from  $n_\infty$ , meaning no plasma interaction occurs there, to zero, meaning all passing stream particles are ionized by the magnetosheath plasma. This interaction with the plasma forms a wake-like structure that extends far beyond the magnet, which contributes to the large effective drag area shown later.

### 2.2 Key Magnetosheath Physics

Propagating the model equations until the system reaches equilibrium, we extract steady-state solution data that is manipulated to reveal physical trends. Recall that the global model couples the hypersonic flow to the plasma mass and energy. The strength of this coupling has significant bearing on the magnetosheath's utilization of the in-situ flow and the resulting drag force. One measure of the strength of the interaction is to compare the characteristic timescale of plasma-flow particle reactions with the characteristic rate at which stream particles transit the magnet [12][13]. We define the dimensionless reaction parameter

$$\zeta^* = \frac{\tau_{\text{res}}}{\tau_{\text{cap}}} \quad (1)$$

as the ratio of the stream particle residence timescale  $\tau_{\text{res}}$  to the stream particle capture (i.e. ionization and charge exchange) timescale  $\tau_{\text{cap}}$ . With this definition, higher values of  $\zeta^*$  correspond to higher rates of flow ionization and confinement. We note that  $\tau_{\text{cap}}$  is defined characteristically at the outermost boundary of trapped ions where the plasma density is lowest in the control volume. Therefore,  $\zeta^*$  represents the minimum reactivity associated with confinement of ionized flow.

Fig. 2 shows the dependence of  $\zeta^*$  on  $u_\infty$  for four different cases of seed plasma injected power  $P_{\text{inj}}$ . We observe that at

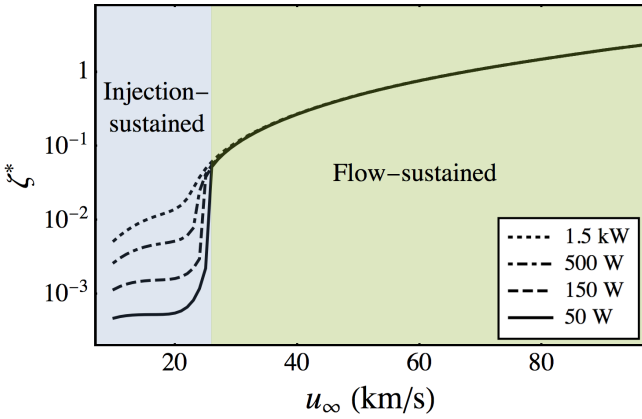


**Figure 2.** The flow/magnetoshell interaction strength,  $\zeta^*$ , increases significantly from the injection-sustained to the flow-sustained regime. Four increasing values of the artificially injected plasma power  $P_{\text{inj}}$  show how it modulates the interaction at low velocity but has negligible effect in the flow-sustained regime. The fixed conditions are  $n_\infty = 10^{18} \text{ m}^{-3}$ ,  $B_0 = 500 \text{ G}$ , and  $r_c = 1 \text{ m}$ .

low velocities, the energy deposited by the artificial plasma source has a significant effect on  $\zeta^*$ . Despite this, the interaction is generally weak ( $\zeta^* \ll 1$ ) as the flow kinetic energy is insufficient to overcome losses from the system in the form of diffusion. There is a sharp velocity threshold where the interaction strength increases by 1-2 orders of magnitude and is no longer affected by  $P_{\text{inj}}$ . This effect results from the well-known ‘‘critical ionization velocity’’ phenomenon (CIV) [16]; flow energy deposited to the plasma heats electrons, energizing them enough to ionize incoming neutrals, thereby increasing plasma density. The increased plasma population begets more ionizing interactions in a feedback effect that results in a steady-state high-density plasma supported by kinetic energy alone.

The transition to this flow-sustained regime has significant implications for the design and use of magnetoshells. To see the effect of the transition on the magnetoshell, in Fig. 3 we plot the rate of mass and energy absorption by the plasma ( $\dot{m}_{\text{cap}}$  and  $P_{\text{cap}}$ , respectively) as a function of magnetic field strength for several freestream densities. Note that this flow capture represents only the amount trapped by the plasma to sustain the interaction; significantly more flow is ionized in regions where it deflects away from the magnet to produce drag, as we show in Section 2.3. Even for a fixed velocity as shown here, the plasma transitions to the high-density mode as  $B_0$  is increased. Before the transition, flow absorption is on the same order as that being artificially injected (50 W, 0.1 mg/s). In the flow-sustained regime, the absorbed power can be tens of kW, implying the magnetoshell utilizes the flow as an in-situ fuel and power source. The consequences of this for the performance of magnetoshells in DMPA missions are now discussed.

### 2.3 Magnetoshell Performance Scaling

A distinguishing feature of aerocapture is the high drag force required to achieve several km/s of  $\Delta v$  in just a few minutes. In magnetoshells, some of this drag results from the momentum absorption associated with the aforementioned capture of flow. However, a majority of momentum transfer occurs outside this ion-trapping region where flow particles are

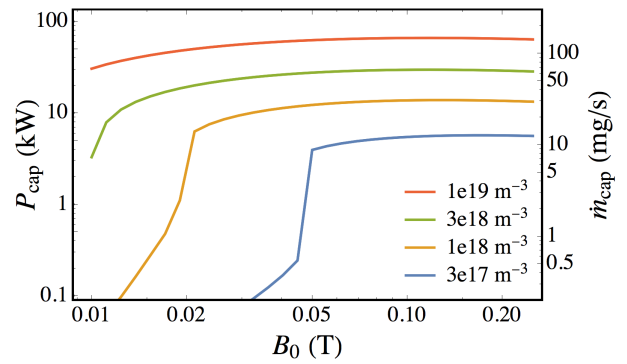


**Figure 3.** The rate of capture of flow energy ( $P_{\text{cap}}$ ) and mass ( $\dot{m}_{\text{cap}}$ ) by the magnetoshell increases significantly in the flow-sustained regime, indicated by the massive jumps as magnetic field strength  $B_0$  is increased. Four freestream particle densities  $n_\infty$  are shown, with higher capture and wider flow-sustained regimes for increasing  $n_\infty$ . The fixed conditions are  $u_\infty = 30 \text{ km/s}$ ,  $r_c = 1 \text{ m}$ , and  $P_{\text{inj}} = 50 \text{ W}$ .

ionized and deflected by the magnetic field. To gain intuition for drag on a magnetized plasma, in Fig. 4 we examine the spatial distribution of momentum transfer resulting from such magnetic interaction. Here we plot the volumetric force that, when integrated over all space, gives the total drag

$$F_D = \int_{\infty} R_{\text{tot}} n_{sn} n_e m_{sn} \Delta u_z dV, \quad (2)$$

where  $R_{\text{tot}}$  is the total plasma-stream reaction coefficient and  $m_{sn}$  is the stream particle mass. The integrand in Eq. (2) is the product of the rate of flow ionization and the resulting deceleration momentum of the ionized particle, where  $\Delta u_z$  is the change in axial velocity of the particle. This manifests in Fig. 4 which shows the force density is highest in front of the magnet and near the coil – where the ionizing reaction primarily occurs and where particles are most deflected by the strong magnetic field, respectively. Fig. 4 also highlights the mechanism by which magnetoshells achieve continuously-variable drag modulation. All other conditions equal, only the magnetic field strength is increased from 0.2 kG in 4(a) to 2 kG in 4(b). We can see that the region of momentum transfer grows much larger as the field strength is increased, and indeed the total drag force increases from  $F_D = 1.4 \text{ kN}$  to  $F_D = 13.1 \text{ kN}$ .

Although the spatial extent of drag on the plasma is clearly large, the interaction is not discrete but rather gradually weakens radially away from the magnet. In order to compare magnetoshell performance with aeroshells, we define an effective surface area

$$(C_{\text{D}} A)_{\text{eff}} = \frac{F_D}{\rho_\infty u_\infty^2 / 2} \quad (3)$$

where  $\rho_\infty = m_{sn} n_\infty$  is the freestream mass density. Eq. (3) normalizes the magnetoshell drag by the freestream dynamic pressure; in this sense,  $(C_{\text{D}} A)_{\text{eff}}$  represents the area of a solid body that would generate a drag force equivalent to that of the diffuse plasma. Fig. 5 shows the effective surface diameter,  $D_{\text{eff}}$  (where  $(C_{\text{D}} A)_{\text{eff}} = \pi D_{\text{eff}}^2 / 4$ ), as a function of  $\rho_\infty$  and  $B_0$ . In the flow-sustained regime, we observe an effective diameter on the order of 10–40 m, significantly larger than

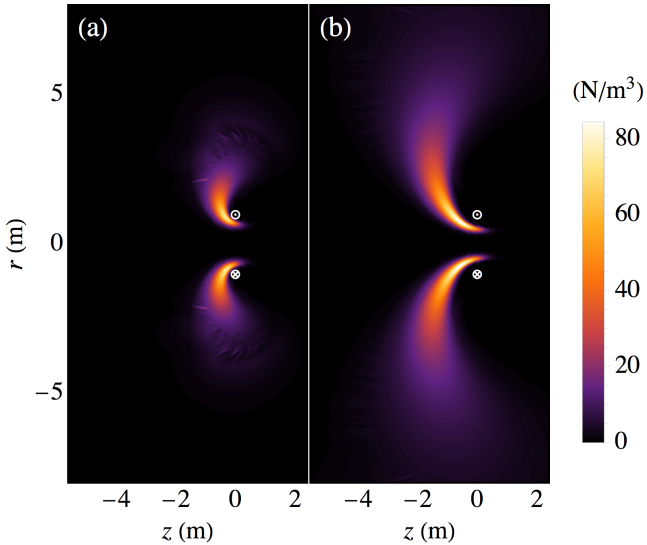


**Figure 4.** A heatmap of the volumetric drag force for (a)  $B_0 = 0.2$  kG and (b)  $B_0 = 2$  kG demonstrates how modulating the magnetic field strength affects the magnetoshell/flow interaction. The fixed conditions are  $n_\infty = 7.5 \times 10^{18} \text{ m}^{-3}$ ,  $u_\infty = 30 \text{ km/s}$ , and  $r_c = 1 \text{ m}$ .

what is achieved by modern-day deployable aeroshells. The injection-sustained regime is apparent in the lower left of the plot as a region of low  $D_{\text{eff}}$ , with the stark transition between the two regimes reflective of the scaling shown in Fig. 3. We highlight two data points corresponding to the force distributions shown in Figs. 4(a) and 4(b) to demonstrate the relationship between the spatially diffuse nature of the momentum transfer interaction and the effective surface area.

Note in Fig. 5 that at a fixed  $\rho_\infty$  and  $u_\infty$ ,  $D_{\text{eff}}$  is a strong function of magnetic field strength. This phenomenon is crucial to DMPA. The freestream density and velocity are entirely functions of the spacecraft trajectory through the atmosphere; therefore, at any given point in the trajectory,  $(C_{\text{DA}})_{\text{eff}}$  can be modulated by order(s) of magnitude via the magnet. The vehicle ballistic coefficient,  $\beta$ , is defined for a spacecraft of mass  $m_{\text{sc}}$  as

$$\beta = \frac{m_{\text{sc}}}{C_{\text{DA}}}. \quad (4)$$

Trajectory studies indicate that the ratio of maximum to minimum  $\beta$  achieved by a drag-modulation decelerator is the strongest driver of final orbit accuracy [4]. Staged jettison aeroshells have typical  $\beta$  ratios of about 10. Because magnetoshells can be deactivated mid-maneuver without jettisoning mass, their  $\beta$  ratio is simply the effective plasma area over the aerocapture vehicle's nominal solid area ( $C_{\text{DA}})_{\text{sc}}$ ,

$$\frac{\beta_{\text{max}}}{\beta_{\text{min}}} = \frac{(C_{\text{DA}})_{\text{eff}}}{(C_{\text{DA}})_{\text{sc}}}. \quad (5)$$

The large effective diameter and the ability to deactivate the magnetoshell can result in order-of-magnitude improvements to  $\beta$  ratio compared to aeroshell drag modulation. Combined with the potential to continuously modulate  $\beta$  through  $(C_{\text{DA}})_{\text{eff}}$ , this represents a significant technological leap in drag-modulation aerocapture. This opens up novel mission applications and imposes unique design constraints that are now discussed.

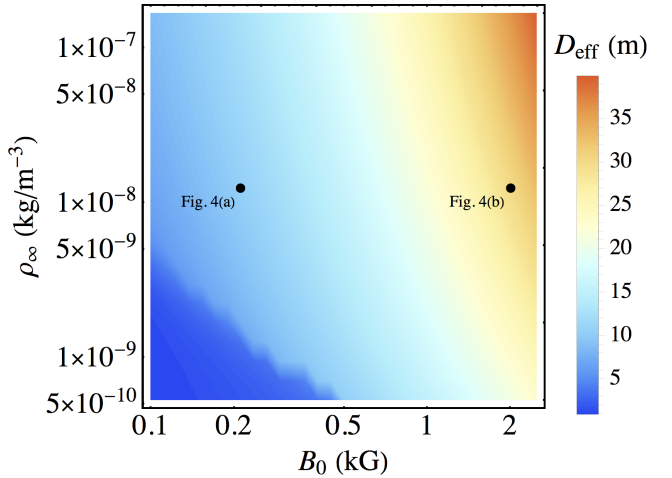


**Figure 5.** The effective drag surface diameter of the magnetoshell,  $D_{\text{eff}}$ , is a strong function of magnetic field strength and can reach tens of meters with only a 2 m-diameter magnet. The two points correspond to the force density plots shown in Fig. 4. The fixed conditions are  $u_\infty = 30 \text{ km/s}$ ,  $r_c = 1 \text{ m}$ , and  $P_{\text{inj}} = 50 \text{ W}$ .

### 3. MISSION DESIGN CONSIDERATIONS

The magnetoshell enabling DMPA is a novel technology with little prior hardware development. Here, we lay out an initial framework that can be used to obtain first-order design scaling of a magnetoshell meeting the needs of a given mission. This framework takes into account notional mission parameters such as entry velocity and  $\Delta v$ ; spacecraft limitations such as size, weight, power, and TPS; and magnetoshell performance parameters such as drag force and controllability. One may use this analysis as a “first pass” to generate a mission design that roughly closes before moving on to a more thorough analysis of hardware requirements and drag modulation trajectories.

#### 3.1 Mission Architecture

Fig. 6 shows the general architecture of a DMPA maneuver. The spacecraft arrives at the atmosphere along a hyperbolic orbit. Once in the atmosphere, the magnetoshell is activated by powering the magnet and injecting plasma to seed interaction with the flow. Like a ballute [17], the device may be fixed to the spacecraft or trailed behind it (depicted in a trailing configuration in Fig. 6). The effective area  $(C_{\text{DA}})_{\text{eff}}$  is modulated continuously by controlling the magnetic field strength during the maneuver. The magnetoshell may also be deactivated during the maneuver by simply unpowering the magnet to return the spacecraft to a ballistic trajectory. This avoids the risk associated with a mechanical separation during hypersonic flight, as in aeroshell-jettisoning drag modulation schemes [18], and enables higher  $\beta$  ratios because there is no vehicle mass lost. Upon exiting the atmosphere, the magnet is released from the spacecraft and ballistically aerobrakes in the next orbit(s) until being destroyed in reentry. Meanwhile, the spacecraft performs any necessary trajectory correction maneuvering to enter its final orbit.

Although significant technological advancement is required to implement DMPA, we aim to leverage contemporary state-of-the-art wherever possible to limit bottlenecks imposed by more advanced concepts. Therefore, we restrict the design

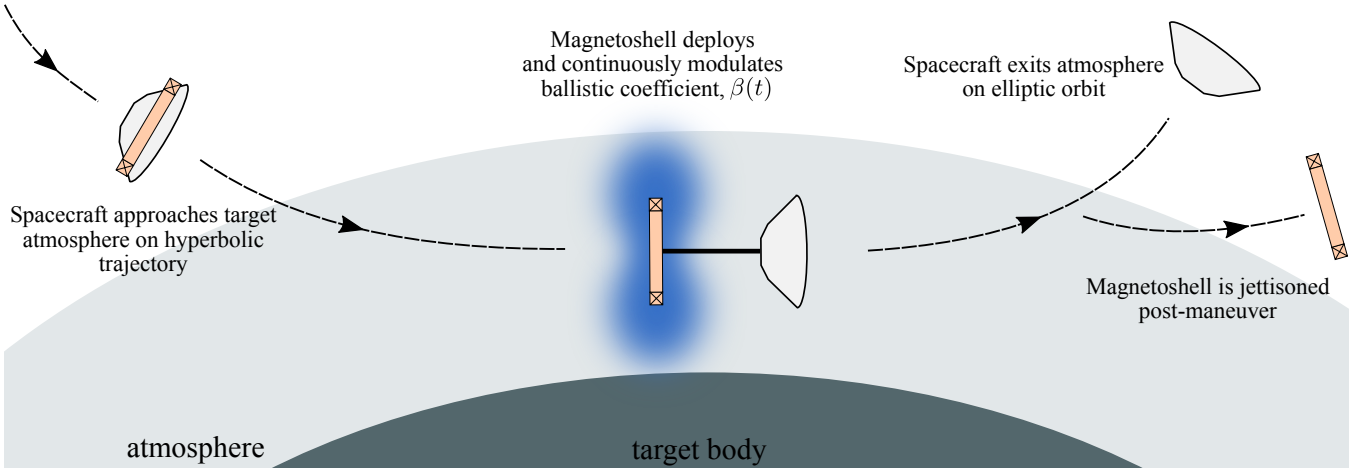


**Figure 6.** Overview of a DMPA maneuver with a trailing magnetoshell configuration.

architecture in the following ways. Large magnets (meters-scale) with high field strengths ( $\sim$ kG) are required to generate sufficient drag for successful aerocapture. A standard electromagnet of aluminum or copper wire is proposed for the magnetoshell. Superconducting magnets can reach these high field strengths, but their implementation in space systems requires significant technological breakthroughs; permanent magnets offer simplicity, but stacking them to achieve the required field strength is mass-prohibitive. While feasible to construct, the electromagnet approach places a high demand on power (ten to hundreds of kW) that cannot be delivered by solar arrays or near-future generators. Instead, a high-energy battery bank is kept charged during cruise and discharged as a power source during the maneuver. A power processing unit (PPU) will be utilized similar to those used in modern electric propulsion spacecraft. Finally, TPS mass is estimated as a fraction of the system mass based on heritage designs. For the purposes of design scaling, we assume these elements (electromagnet, batteries, PPU, and TPS) mainly comprise the architecture and impose the biggest constraints on mass, size, and technology development.

### 3.2 DMPA Design Scaling

The goal of this framework is to produce a first order magnetoshell design that (1) has the desired performance for the given destination and (2) closes with modern technology constraints. A fundamental determinant of performance needs for an interplanetary orbiter is the  $\Delta v$  of the insertion maneuver. We roughly estimate the average drag force necessary for a given DMPA maneuver,  $F_{D,\text{avg}}$ , as

$$F_{D,\text{avg}} = \frac{m_{\text{sc}} \Delta v}{\Delta t_{\text{atm}}} \quad (6)$$

where  $\Delta t_{\text{atm}}$  is the time spent in the sensible atmosphere. The mass of the vehicle delivered to the target pre-maneuver ( $m_{\text{sc}}$ ) is largely a function of the launch vehicle and trajectory design, whereas  $\Delta t_{\text{atm}}$  depends on the destination and can be estimated based on existing aerocapture simulations. The magnetoshell must be designed to the maximum drag force that will be required during the maneuver, which we estimate as  $F_{D,\text{max}} \approx 3F_{D,\text{avg}}$ . The analytical model can then be used to determine combinations of input conditions that can produce this drag, forming the magnetoshell design space.

Any number of different magnet designs may be able to

attain  $F_{D,\text{max}}$ . However, the design must not only meet the performance goal but also be optimized for diameter, power, mass, and overheating avoidance. The magnet consists of wire wound circularly with  $N$  total turns. A magnet of average radius  $r_c$  produces a magnetic field at its center of

$$B_0 = \frac{\mu_0 N I}{2r_c} \quad (7)$$

where  $I$  is the applied current through the wire. The power  $P_m$  required to drive the magnet current is ohmic, i.e.  $P_m = I^2 R$ . The current  $I$  and total resistance  $R$  can be tuned by adjusting the wire gauge/material and parallelizing multiple loops. However, our design space is driven from simulations dictating  $r_c$  and  $B_0$  and mission constraints dictating the mass. We therefore cast the power requirement in terms of these parameters.

The mass of the magnet coil,  $m_c$ , is given by

$$m_c = l_w A_w \rho_w \quad (8)$$

where  $l_w$  is the overall wire length,  $A_w$  is the wire cross-sectional area (i.e. gauge selection), and  $\rho_w$  is the mass density of the wire (i.e. material selection). The total resistance of the winding is

$$R = \frac{l_w}{A_w \sigma_w} \quad (9)$$

where  $\sigma_w$  is the wire conductivity. Assuming  $r_c$  is the average coil radius regardless of its overall thickness, the wire length is given by

$$l_w = 2\pi r_c N. \quad (10)$$

Finally, Eqs. (7)–(10) are combined to give the magnet power,

$$P_m = I^2 R = \left(\frac{4\pi}{\mu_0}\right)^2 \frac{B_0^2 r_c^4 \rho_w}{m_c \sigma_w}. \quad (11)$$

Note this equation couples several magnet design parameters (power, size, strength, mass, and material selection) while being agnostic to the electrical design (current, voltage, series-parallel configuration). Crucially, this enables straightforward design optimization of the basic mission architecture described in Section 3.1.

The power requirement given by Eq. (11) subsequently drives the battery and PPU designs. For this first-order design, we are primarily concerned with the mass and volume of these elements to ensure they can reasonably fly aboard the aerocapture vehicle. We compute the battery energy storage requirement assuming the maximum power  $P_m$  is applied for the full duration of  $\Delta t_{\text{atm}}$  and applying a 2x margin. For gravimetric and volumetric battery energy densities  $\alpha_{b,g}$  and  $\alpha_{b,V}$ , respectively, the battery mass and volume are estimated as

$$m_b = 2\alpha_{b,g}P_m\Delta t_{\text{atm}}, \quad (12)$$

$$V_b = 2\alpha_{b,V}P_m\Delta t_{\text{atm}}. \quad (13)$$

Similarly, the PPU mass  $m_{\text{ppu}}$  is a function of the max power requirement. Assuming a specific mass of  $\alpha_{\text{ppu}}$ , we have

$$m_{\text{ppu}} = \alpha_{\text{ppu}}P_m. \quad (14)$$

The final check is to ensure ohmic dissipation will not internally overheat the magnet. We estimate the magnet heating rate  $\dot{T}_m$  as

$$\dot{T}_m = \frac{P_m}{m_c c_p} \quad (15)$$

where  $c_p$  is the heat capacity of the wire material. With  $P_m$  a function of  $B_0$ ,  $r_c$ , and  $m_c$ , the magnetosheath system is easily optimized for the minimum total mass  $m_{\text{tot}}$  satisfying the design requirements. We estimate this as the sum of the three main elements,

$$m_{\text{tot}} = 1.5(m_c + m_b + m_{\text{ppu}}), \quad (16)$$

where a 50% margin is applied to conservatively account for the structural mass associated with the magnetosheath system.

To see how the above framework enables optimized design considerations, we examine different magnetosheath configurations that have identical discharge power requirements,  $P_m = 100$  kW, and coil masses,  $m_c = 1200$  kg. Assuming aluminum wire ( $\rho_w = 2700$  kg/m<sup>3</sup>,  $\sigma_w = 3.77 \times 10^7$  S/m), Eq. (11) dictates a locus of magnet diameters  $d_c = 2r_c$  and strengths  $B_0$  satisfying the power and mass constraints. In Fig. 7, we show  $(CDA)_{\text{eff}}$  as a function of flow velocity and density (mapped to Neptune altitude) for four such magnet configurations. We observe that, for equal power and coil mass, larger diameter magnets with weaker fields are capable of significantly higher effective drag area than small magnets with strong fields. Recall that higher  $\beta$  ratio yields better orbit targeting accuracy and that the denominator in Eq. (5) is fixed. Thus, Fig. 7 clearly demonstrates this design should be optimized for maximum magnet size. The freestream density  $n_\infty$  is correlated to an altitude at Neptune using Eq. (19) and the Neptune-GRAM-derived density profile given by the open-source Aerocapture Mission Analysis Tool (AMAT) [19]. These plots therefore represent a “flight envelope” performance map for Neptunian DMPA for these specific magnetosheath designs. We see the transition to the flow-sustained regime clearly defines the region of applicability to  $u_\infty > 15$  km/s at the least, a threshold that increases with altitude. This again highlights that the impact of the critical ionization physics discussed in Section 2.2 is to restrict DMPA to high-velocity applications, motivating the consideration of outer planet missions.

### 3.3 Example Mission Design

Using the design framework presented in the previous section, we can generate preliminary DMPA mission designs

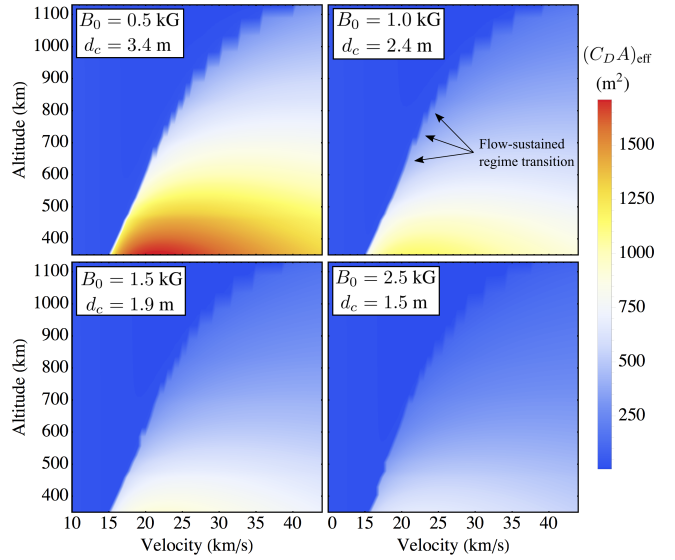


**Figure 7.** Maximum effective drag area,  $(CDA)_{\text{eff}}$ , in Neptune’s atmosphere for four magnet strengths ( $B_0$ ) and diameters ( $d_c$ ). The magnet mass,  $m_c = 1200$  kg, and magnet power,  $P_m = 100$  kW, are equal for all four cases, highlighting the incentive to maximize  $d_c$ .  $(CDA)_{\text{eff}}$  can be over  $1500$  m<sup>2</sup>, providing a high degree of  $\beta$  control. The flow-sustained threshold demonstrates a clear lower bound on spacecraft velocity defining the Neptune flight envelope.

for given sets of constraints. Here we use a Neptune orbiter mission concept developed by JPL and NASA Ames [2][20] as a reference point for constraints and comparison. This drag-modulation aerocapture (DMA) mission would deliver an aerocapture vehicle with mass  $m_{\text{sc}} = 5,725$  kg to the atmospheric interface at Neptune. The vehicle consists of a 4 m-diameter capsule with an attached 12 m-diameter ADEPT drag skirt that is jettisoned during the maneuver in a single-event drag modulation scheme. The skirt stows during launch concentrically around the rear of the capsule to fit within a 5 m fairing. The ADEPT skirt has a mass of 3,145 kg with an additional 1,100 kg of heat shielding on the capsule so that the final payload mass delivered to orbit is 1,480 kg [2]. One of the significant advantages of the mission is the potential to reduce trip time to Neptune from 12-13 years using an all-propulsive architecture to 9 years using aerocapture.

In order to compare DMPA design and performance with the ADEPT concept, we first select some representative mission constraints given by [2]. The entry velocity is 25 km/s with respect to the atmosphere, the time spent in the sensible atmosphere is  $\Delta t_{\text{atm}} = 350$  s, and the required  $\Delta v$  is about 5.5 km/s. From this we estimate a drag force requirement of  $F_{D,\text{max}} \approx 270$  kN as a design point for magnetosheath performance. Recall from Fig. 7 that effective drag area scales most strongly with  $r_c$ ; therefore we set  $r_c = 2$  m to make full use of the payload volume. The ADEPT vehicle experiences a peak stagnation heat flux of about 170 W/cm<sup>2</sup>, which we use as an upper constraint for the DMPA trajectory design. With a nose radius  $R_n = 1$  m and assuming the max stagnation heating occurs about halfway through the maneuver ( $u_\infty \approx 22.25$  km/s), we find the maximum allowable atmospheric density  $n_{\infty,\text{max}} \approx 10^{21}$  m<sup>-3</sup> from the Sutton-Graves heating equation [21]. In practice, this sets a minimum periapsis altitude. We have therefore constrained the value of three parameters at

**Table 1.** System design comparison between the Neptune DMA mission architecture using an ADEPT drag skirt and a magnetoshell. ADEPT values are taken directly (or calculated) from [2]. Magnetoshell values are calculated for the trajectory shown in Fig. 8.

Neptune DMA system	w/ ADEPT	w/ Magnetoshell
Modulation scheme	Single-stage	Continuous
A/C system mass	3145 kg	2130 kg
TPS mass	1100 kg	1100 kg
Payload mass	1480 kg	2495 kg
Peak heat flux	170 W/cm <sup>2</sup>	120 W/cm <sup>2</sup>
Total heat load	40 kJ/cm <sup>2</sup>	22 kJ/cm <sup>2</sup>
Peak dynamic pressure	2.8 kPa	0.3 kPa
$C_{DA}$	190 m <sup>2</sup>	1430 m <sup>2</sup>
Minimum $\beta$	30 kg/m <sup>2</sup>	4 kg/m <sup>2</sup>
$\beta$ ratio	4	67
$m_c$	n/a	710 kg
$P_m$	n/a	105 kW
$B_0$	n/a	250 G

the design point ( $r_c$ ,  $u_\infty$ , and  $n_\infty$ ) that are all inputs to the analytical plasma model presented in Section 2.

The next step is to run simulations of the magnetoshell/flow interaction with these fixed inputs and an array of magnetic field strengths,  $B_0$ . From the model results, we determine a requirement on  $B_0$  of 50 G to achieve the drag force  $F_{D,\max}$  at the design point. (An open-source dataset of the plasma model performance results is available for download [here](#).) Recall from the previous section that our magnetoshell design space consists of  $m_c$ ,  $r_c$ , and  $B_0$ , the latter two of which have been prescribed. We now optimize for minimum total system mass  $m_{\text{tot}}$  via the coupled Eqs. (11), (12), (14), and (16). We assume aluminum wire is used for the magnet winding; the battery energy density is that of modern Li-ion cells,  $\alpha_{b,g} = 250 \text{ Wh/kg}$  [22]; and the PPU specific mass scales as a modern electric propulsion unit,  $\alpha_{\text{ppu}} = 6 \text{ kg/kW}$  [23]. The minimum total mass is  $m_{\text{tot}} = 430 \text{ kg}$  with a coil mass of  $m_c = 142 \text{ kg}$  and a discharge power of  $P_m = 21 \text{ kW}$ . The ohmic heating rate from Eq. (15) is  $\dot{T}_m \approx 10 \text{ }^{\circ}\text{C}/\text{min}$ , posing no risk of internally overheating the magnet.

Contrasted with the ADEPT system mass of 3,145 kg, this result suggests an overwhelming improvement in final orbiter mass by using a 4 m-diameter, 50 G magnetoshell. However, this magnetic field is very weak; recall that the flow-sustained regime collapses below a certain field strength, and 50 G is near the edge of validity for the plasma model itself. At a max  $B_0$  of 50 G, there is also only a small range to vary the field for continuous drag modulation. One mitigation is to simply increase the system power, as there is plenty of mass margin to enhance this design. However, we can also assess the use of magnetoshells to ease other challenging constraints. For instance, we used 170 W/cm<sup>2</sup> as a constraint on stagnation heating, but the large effective diameter suits magnetoshells for use higher in the atmosphere to reduce heat load to the spacecraft. Restricting the design to  $B_0 > 200 \text{ G}$ , we find the system mass is minimized for a design point stagnation heating of 120 W/cm<sup>2</sup>. The system design and performance parameters for this case are given in Table 1. We assume the magnetoshell vehicle requires the same TPS mass as the ADEPT vehicle, though in practice it may be less due to the reduced heat load [24].

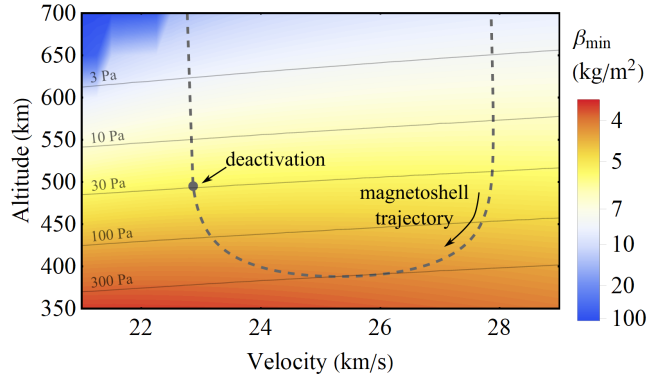


**Figure 8.** Map of best magnetoshell  $\beta$  for the flight envelope in Neptune’s atmosphere using the DMPA architecture given in Table 1. Gray contours are level curves of dynamic pressure. The dashed gray curve shows a DMPA trajectory calculated with a drag force corresponding to the  $\beta_{\min}$  shown.

A performance map of the magnetoshell design described in Table 1 is shown in Fig. 8. Here we plot the minimum ballistic coefficient  $\beta_{\min}$  achieved by the magnetoshell [corresponding to its maximum ( $C_{DA}$ )<sub>eff</sub>]. We also plot a DMPA trajectory that is propagated using the equations of motion for a spacecraft inside the atmosphere of an ellipsoidal rotating planet [25][26]. In this propagation, the drag force along the entire trajectory is the actual magnetoshell drag, calculated from Eq. (2) and implemented using a lookup table and interpolation. The magnetoshell is deactivated near the end of the atmospheric pass and the spacecraft exits with an apoapsis of 340,000 km. We note that there is no modulation in this case; the magnet is maintained at the max field strength of 250 G, although the model is still in progress with plans to implement continuous drag modulation. In addition to the reduced heat flux, we observe the dynamic pressure is reduced by an order of magnitude by flying at a higher altitude; ADEPT has a peak around 3 kPa while the periapsis of the magnetoshell trajectory reaches about 300 Pa. Along the entire trajectory the magnetoshell can achieve single-digit  $\beta_{\min}$  values, with a best of  $\beta_{\min} = 4$ . The magnetoshell can be powered off without jettisoning it, so the maximum  $\beta$  is higher ( $\beta_{\max} \approx 270 \text{ kg/m}^2$ ) than that for the ADEPT case ( $121 \text{ kg/m}^2$ ), which necessarily loses vehicle mass in the modulation event. Thus, this DMPA architecture can achieve an unprecedented  $\beta$  ratio of 67. We reiterate that not only is there a large ratio of highest to lowest ballistic coefficients, it is also continuously controllable between these two extremes.

While we chose to design to an existing mission concept in this example, there are myriad ways to utilize the design framework presented here. For example, one can design a mission for minimizing discharge power in order to take PPU technology constraints into account. In this case, one would (1) select velocity and density design points based on the mission parameters and heat flux constraint; (2) determine a locus of  $r_c$  and  $B_0$  combinations that satisfy the drag requirement; (3) find the  $(r_c, B_0)$  combination that minimizes  $P_m * m_c$ , then; (4) compute the  $m_c$  that minimizes  $P_m$  subject to a constraint on  $m_{\text{tot}}$  (or, alternatively, the  $m_c$  that minimizes  $m_{\text{tot}}$  subject to  $P_m$  constraint). The model may also be refined and built upon to take other effects into account such as total heat load constraint, heat shield mass

**Table 2.** Sample design of the magnet presented for the Neptune DMPA mission described in Table 1.

Parameter	Value
Discharge power	105 kW
Wire gauge	5 AWG
Wire material	Aluminum
Total turns, $N$	1242
Coil thickness	15 cm
# of Parallel coils	6
Turns/coil	207
Current/coil	64 A
Voltage	262.5 V
Total # of 18650B batteries	1604
Battery configuration	72s22p
Battery discharge rate	5.4C
Battery volume	28U
Self-inductance, $L$	34.3 H
Time constant, $\tau_{RL}$	1.4 s

scaling, less conservative energy storage requirement, etc.

#### 3.4 Additional Considerations

Finally, we consider some details of the implementation of such a magnetoshell design to ensure it is feasible. In the framework presented above, we explicitly omitted consideration of the electrical configuration of the magnet and battery system to focus on a few key mission design parameters. However it is relevant to check whether such a magnet can be operated within the technical limits of its components. We show in Table 2 that the magnet designed for the mission described in Table 1 and Fig. 8 can be built using an arrangement of six electrically parallel windings each receiving 64 A of current. This is achieved with 22 parallel strings of 72 Li-ion batteries each that discharge at 5.4x their nominal capacity, which is safe for this battery chemistry and for this single-use application. The volume occupied by a battery bank of this size is 28U (where 1U = 1 L) based on the volumetric energy density  $\alpha_{b,V} = 680 \text{ Wh/L}$  [22]. It is worth mentioning that there is no available space-ready PPU that can handle the 105 kW battery discharge employed by this magnetoshell. However, the NASA NextSTEP partnership has led to development of a PPU capable of supporting a 200 kW nested Hall thruster [27]. This PPU has been demonstrated up to 66 kW output steady-state and 87.7 kW peak as of 2019, on track to eventually support power outputs in excess of 250 kW. We therefore do not anticipate PPU advancement being a bottleneck for magnetoshell technology development.

Another consideration for magnetoshell applicability is how easily the magnetic field can be modulated. This affects the design of a drag-modulation feedback controller that will drive a current through the magnet as an actuator. A magnet of this size and weight can have significant self-inductance that acts to inhibit rapid changes to the flow of current. In practice, this means that the response of the magnet to a control input is delayed on a timescale that may be significant compared to the maneuver duration. We therefore characterize the time constant of the system by considering the magnet as a simple RL circuit. In terms of the magnet design parameters, the inductance and circuit time constant

are calculated as

$$L = \frac{\mu_0 m_c^2}{4\pi^2 \rho_w^2 A_w^2 r_c} \left[ \ln\left(\frac{8r_c}{\sqrt{A_w/\pi}}\right) - 2 \right], \quad (17)$$

$$\tau_{RL} = \frac{L}{R} = \frac{\mu_0 m_c \sigma_w}{4\pi^2 r_c \rho_w} \left[ \ln\left(\frac{8r_c}{\sqrt{A_w/\pi}}\right) - 2 \right] \quad (18)$$

Notice that unlike the previous magnet design parameters,  $L$  does depend on the choice of wire gauge. However, the value of  $\tau_{RL}$  only increases 30% between 0 AWG and 20 AWG wire so the choice is more strictly driven by ampacity and coil configuration considerations. For the Neptune DMPA design in Table 2, the time constant is  $\tau_{RL} = 1.4 \text{ s}$ . This is negligible on the time scale of the aerocapture maneuver (350 s). However, this may have implications for the ability of the magnetoshell to respond to rapid atmospheric disturbances. Also, smaller magnets or those with more windings can reasonably have response times on the order of 10 s, which must be taken into consideration in the design of a feedback controller for continuous drag modulation.

The system design is strongly driven by the magnetoshell performance scaling, which depends on the results of the analytical plasma model. Recall that this model only describes the interaction of atomic hydrogen flow and plasma. A molecular hydrogen model is in development, and while the performance scaling is not anticipated to change drastically, we briefly describe here how we extrapolate results of atomic modeling to the Neptunian atmosphere (or any other predominantly H<sub>2</sub> atmosphere). Assuming that the H atoms impacting the magnetoshell result from electron dissociation of H<sub>2</sub> in the flow, the number density of H,  $n_\infty$ , is correlated to the mass density of the local atmosphere  $\rho_{atm}$  by

$$n_\infty = 2f_{H_2} \frac{\rho_{atm}}{\bar{M}_{atm} m_p} \quad (19)$$

where  $f_{H_2}$  is the fraction of H<sub>2</sub> by volume,  $\bar{M}_{atm}$  is the mean molecular weight of the atmosphere, and  $m_p$  is the proton mass. This is a broad simplification that neglects plasma chemistry, other significant species (such as He which has  $f_{He} = 0.19$  at Neptune), and the dependence of composition on altitude. Ultimately, the DMPA design scaling will take these into account with a comprehensive plasma simulation and the use of planetary -GRAM models for accurate representation of the freestream flow.

We conclude by re-iterating that magnetoshells are still low-TRL. Past work has attempted to demonstrate technological feasibility in the lab with some positive results [10][28]. However, the device has never been tested in a representative environment and therefore the key physics such as neutral drag on a dipole plasma and critical ionization sustainment of the magnetoshell are unproven experimentally. A technology demonstration experiment is in development at the University of Washington SPACE Lab that will immerse a subscale magnetoshell plasma in a hypersonic, rarefied neutral flow seeking to observe some of these crucial physics. Ultimately, more advanced experimental facilities and significant investment in technology development are required for magnetoshells to reach space readiness.

## 4. CONCLUSION

The design framework presented here is intended as a tool for any engineer to generate basic DMPA architectures for

trade studies of potential deep space missions. To this end, we have published a downloadable dataset of results from the analytical plasma model to facilitate its use by those without a plasma physics background. This is found online [here](#) and will be updated with new results as the analytical model is refined for accuracy and complexity. These data are useful both as a scaling tool and as a lookup table in trajectory simulation codes so that continuous drag-modulation control can be implemented and analyzed.

Detailed design of a DMPA mission will ultimately require more advanced considerations. For instance, the flight configuration of the magnetoshell still remains an open question. A trailing magnetoshell will require significant technology development to release a tethered, several-ton coil and maintain stability in flight; meanwhile, a magnet clamped to the vehicle may suffer performance degradation due to the loss of plasma energy to the spacecraft surfaces. Similarly, for planets with a magnetosphere, a large magnet could produce a non-negligible torque on the order of  $1\text{--}100 \text{ Nm}$ . It is expected that the massive drag force will keep the craft stable, but detailed vehicle-specific analysis is needed to determine if additional measures are required to maintain attitude stability in the presence of this disturbance. The DMPA scaling similarly does not consider TPS implementation for the trailed magnet, the effect of magnet temperature on performance, the reduced mass of capsule heat shielding for higher altitudes, the effect of the craft's wake on plasma/flow interaction, and tuning the design to specific trajectories, among other things. Despite its simplicity, this framework provides a useful starting point for the consideration of DMPA in mission design and will inform technology development toward eventual flight implementation of magnetoshells.

## ACKNOWLEDGMENTS

We wish to thank Alex Austin and Marcus Lobbia for their advice in the development of this model. We thank Bob Moses for continued support of and productive conversations on DMPA. This work was supported by a NASA Space Technology Research Fellowship.

## REFERENCES

- [1] Jeffery L. Hall, Muriel A. Noca, and Robert W. Bailey. Cost-Benefit Analysis of the Aerocapture Mission Set. *Journal of Spacecraft and Rockets*, 42(2):309–320, 2005.
- [2] P. Wercinski, A. Austin, A. Nelessen, B. Strauss, K. Hogstrom, D. Landau, E. Luthman, J. Ravich, M. Lobbia, G. Allen, A. Cassell, D. Prabhu, B. Yount, and E. Venkatapathy. A Neptune Orbiter Concept using Drag Modulated Aerocapture (DMA) and the Adaptable, Deployable Entry and Placement Technology (ADEPT). In *Outer Planets Assessment Group Meeting*, 2019.
- [3] G. Falcone, J. W. Williams, and Z. R. Putnam. Assessment of aerocapture for orbit insertion of small satellites at Mars. *Journal of Spacecraft and Rockets*, 56(6):1689–1703, 2019.
- [4] Zachary R. Putnam and Robert D. Braun. Drag-Modulation Flight-Control System Options for Planetary Aerocapture. *Journal of Spacecraft and Rockets*, 51(1):139–150, Jan 2014.
- [5] John Slough, David Kirtley, and Anthony Pancotti. Plasma Magnetoshell for Aerobraking and Aerocapture. In *32nd International Electric Propulsion Conference*, Wiesbaden, Germany, 2011.
- [6] Kazuhiko Yamada, Yasunori Nagata, Takashi Abe, Kojiro Suzuki, Osamu Imamura, and Daisuke Akita. Suborbital reentry demonstration of inflatable flare-type thin-membrane aeroshell using a sounding rocket. *Journal of Spacecraft and Rockets*, 52(1):275–284, 2015.
- [7] R. Keith Johnson, F. McNeil Cheatwood, Anthony M. Calomino, Stephen J. Hughes, Ashley M. Korzun, John M. Dinonno, and Mike C. Lindell. HIAD Advancements and Extension of Mission Applications. In *International Planetary Probe Workshop*, Laurel, MD, 2016.
- [8] Alan M. Cassell, Paul F. Wercinski, Ethiraj Venkatapathy, Michael Aftosmis, and Michael C. Wilder. Adaptive Deployable Entry Placement Technology (ADEPT) Development for Small Sat Class Venus Missions. In *Venus Exploration Analysis Group 16th Meeting*, Laurel, MD, 2018.
- [9] Sean M. Hancock, Robert W. Moses, and Christopher Goyne. Magnetoshell Aerocapture Performance Opportunities at Mars. In *2018 AIAA SPACE and Astronautics Forum and Exposition*, number September, pages 1–14, 2018.
- [10] David Kirtley. A Plasma Aerocapture and Entry System for Manned Missions and Planetary Deep Space Orbiters. Technical report, 2014.
- [11] Charles L. Kelly and Justin M. Little. Energy and Mass Utilization During Drag-Modulated Plasma Aerocapture. In *2019 IEEE Aerospace Conference*, Big Sky, MT, 2019.
- [12] Justin Little and Charles L. Kelly. Neutral flow interaction with a magnetic dipole plasma: I. Theory and scaling. *Physics of Plasmas*, 27(11):113512, 2020.
- [13] Charles L. Kelly and Justin M. Little. Neutral flow interaction with a magnetic dipole plasma: II. Global modeling. *Physics of Plasmas*, 27(11):113511, 2020.
- [14] Charles L. Kelly and Justin M. Little. Performance Scaling and Mission Applications of Drag-Modulated Plasma Aerocapture. In *36th International Electric Propulsion Conference*, Vienna, 2019.
- [15] Thomas R. Spilker, Mark Adler, Nitin Arora, Patricia M. Beauchamp, James A. Cutts, Michelle M. Munk, Richard W. Powell, Robert D. Braun, and Paul F. Wercinski. Qualitative Assessment of Aerocapture and Applications to Future Missions. *Journal of Spacecraft and Rockets*, pages 1–10, 2018.
- [16] Nils Brenning. Review of the CIV phenomenon. *Space Science Reviews*, 59:209–314, 1992.
- [17] Reuben R. Rohrschneider and Robert D. Braun. Survey of Ballute Technology for Aerocapture. *Journal of Spacecraft and Rockets*, 44(1):10–23, 2007.
- [18] Michelle McClary and Zachary R. Putnam. Assessment of Hypersonic Separation Dynamics For Drag Modulation Systems at Mars. In *AIAA SciTech Forum*, Virtual Event, 2021.
- [19] Athul P. Girija. Aerocapture Mission Analysis Tool (AMAT), 2019.
- [20] E. Venkatapathy, A. Austin, A. Cassell, D. Ellerby, J. Elliott, P. Gage, M. Lobbia, A. Nelessen, D. Prabhu, B. Strauss, and P. Wercinski. Enabling Entry Technolo-

- gies for Ice Giant Missions. In *Ice Giants Systems*, page 2020, London, UK, 2020.
- [21] Kenneth Sutton and Jr. Graves, Randolph A. A general stagnation-point convective-heating equation for arbitrary gas mixtures. Technical report, Langley Research Center, Hampton, VA, 1971.
  - [22] Panasonic. Lithium Ion NCR18650B Datasheet, 2012.
  - [23] Richard R. Hofer, Benjamin A. Jorns, James E. Polk, Ioannis G. Mikellides, and John Steven Snyder. Wear test of a magnetically shielded Hall thruster at 3000 seconds specific impulse. *33rd International Electric Propulsion Conference*, pages 1–24, 2013.
  - [24] Elizabeth Kolawa. Extreme Environments Technologies for Future Space Science Missions. Technical report, NASA Jet Propulsion Laboratory, Pasadena, CA, 2007.
  - [25] Ping Lu, Christopher J. Cerimele, Michael A. Tiggess, and Daniel A. Matz. Optimal Aerocapture Guidance. *Journal of Guidance, Control, and Dynamics*, 38(4):553–565, 2015.
  - [26] N. X. Vinh. *Optimal Trajectories in Atmospheric Flight.*, volume 1. 1982.
  - [27] Sarah W.H. Shark, Scott J. Hall, Benjamin A. Jorns, Richard R. Hofer, and Dan M. Goebel. High power demonstration of a 100 kW nested hall thruster system. In *AIAA Propulsion and Energy Forum and Exposition, 2019*, Indianapolis, IN, 2019.
  - [28] David Kirtley. ISS Launched CubeSat Demonstration of Variable-Drag Magnetoshell Aerocapture: Phase I Final Report. Technical report, 2014.

## BIOGRAPHY



**Charles L. Kelly** is a NASA Space Technology Research Fellow and a PhD candidate in the department of Aeronautics & Astronautics at the University of Washington. He received his MS in Aeronautics & Astronautics from the University of Washington in 2018 and his BSE in Mechanical and Aerospace Engineering from Princeton University in 2014.



**Justin M. Little** is an Assistant Professor in the department of Aeronautics & Astronautics at the University of Washington and director of the SPACE Lab. He received his PhD in Mechanical and Aerospace Engineering from Princeton University in 2014 and his BS in Physics and Aerospace Engineering from the University of California Irvine in 2008.